Supplementary Materials for

Solid–Solid Catalysis in Sustainable Alloy Synthesis

Xinren Chen, Baptiste Bienvenu, Tingting Yang, Baptiste Gault,

Shaolou Wei*, Xuyang Zhou* and Dierk Raabe*

This PDF file includes:
Tables S1 and S2
Figs. S1 to S7

Supplementary Tables:

H_P (eV)	DFT GGA-PBE	DFT metaGGA-r^{2}SCAN
Ni / Fe	-0.23	-0.79
Ni / Fe_2O_3	+1.26	+1.60
Ni / Fe_3O_4	+0.56	-0.12
Ni / FeO	+0.55	-0.26
NiO / Fe	-0.36	-0.40
NiO / Fe_2O_3	+1.15	+1.99
NiO / Fe_3O_4	+0.42	+0.27
NiO / FeO	+0.26	+0.13

Table S1. DFT-predicted partitioning enthalpies H_P between metallic Ni, Fe, and their respective oxides, namely NiO, Fe_2O_3, Fe_3O_4 and FeO. Results of both DFT GGA-PBE and metaGGA-r^{2}SCAN are indicated.

H_P (eV)	DFT GGA-PBE	DFT metaGGA-r^{2}SCAN
Bulk Ni/FeO	+0.55	-0.26
$\{111\}_{Fe}$	+0.28	+0.25
$\{111\}_{O}$	+0.19	-0.21

Table S2. DFT-predicted partitioning enthalpies H_P for the two bulk FCC Ni and FeO, as well as at the {111} interface between FCC Ni and FeO. Results of both DFT GGA-PBE and metaGGA-r^{2}SCAN are indicated, for both the Fe and O-terminated configuration of the interface

Supplementary Figures:

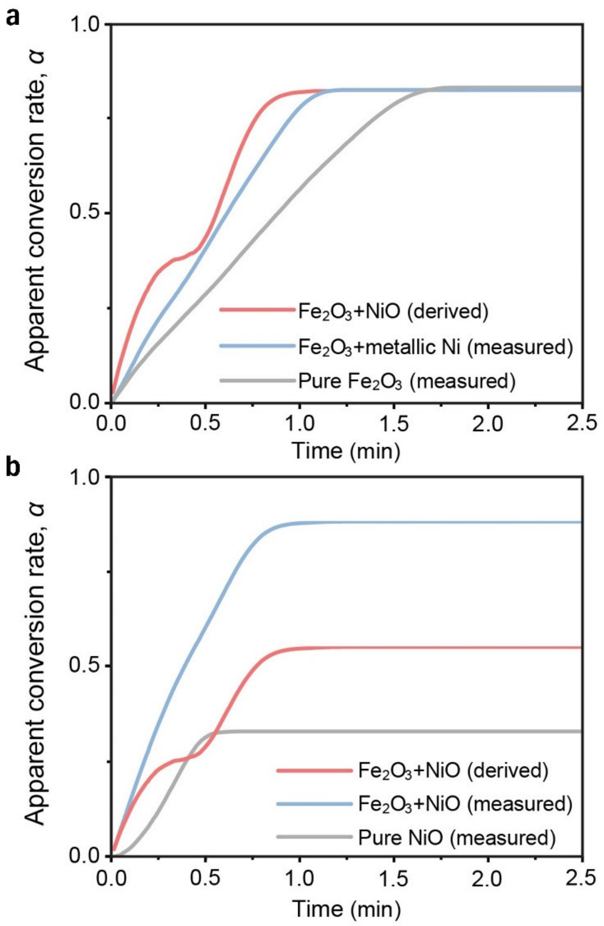

Fig. S1. (**a**) Measured reduction of pure NiO and Fe_2O_3+ NiO (Fe–36Ni wt.%) at 700 °C under a 10 L/h H_2 flow, together with the derived contribution of Fe_2O_3 reduction obtained by subtracting the scaled portion of NiO reduction from the Fe_2O_3 + NiO curve. (**b**) Comparison of measured reduction kinetics of pure Fe_2O_3 and Fe_2O_3 + metallic Ni (Fe–36 wt.% Ni) with the derived contribution of Fe_2O_3 reduction for Fe_2O_3 + NiO (Fe–36Ni wt.%), where the influence of NiO reduction is subtracted, serving as the reference for Fig. 1b.

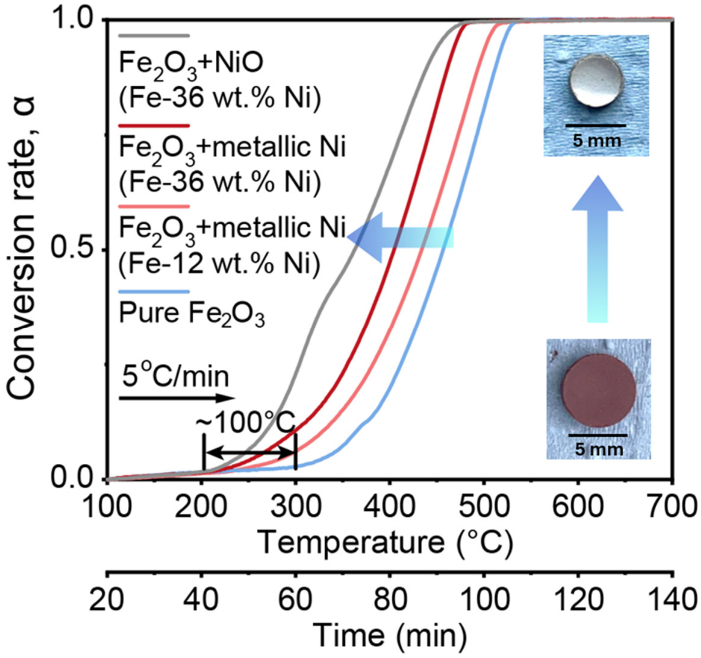

Fig. S2. Conversion curves of Fe_2O_3 reduction (bulk sample) during continuous heating to 700°C under 10 L/h H_2 flow: Ni and NiO addition lowers the reduction temperature and accelerates the reaction. Insets show the morphology of the samples before and after reduction.

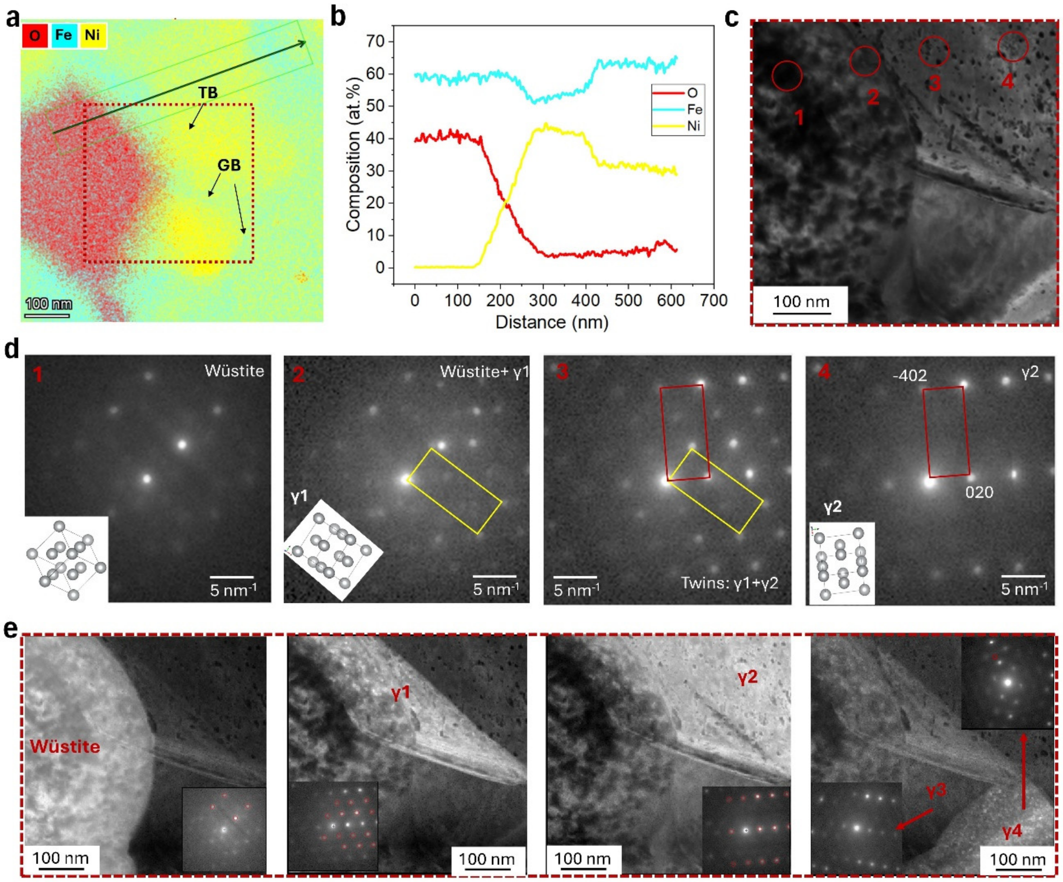

Fig. S3. (**a**) EDS map of Fig. 2e, highlighting elemental distributions of oxygen (O, red), iron (Fe, blue), and nickel (Ni, yellow). Twin boundaries (TB) and grain boundaries (GB) within the Fe–Ni FCC are indicated by arrows. (**b**) EDS line profile taken from (a), showing a compositional transition at the $Fe_{1-x}O$/FCC interface. (**c**) Magnified virtual bright-field 4D-STEM image of the region outlined in Fig. 3a, with four indicated positions (1–4) selected for selected area electron diffraction (SAED) analysis. (**d**) SAED patterns from positions 1–4 in (c), confirming (1) $Fe_{1-x}O$, (2) a mixed $Fe_{1-x}O$–FCC diffraction pattern, (3) twinned FCC reflections (γ1+γ2), and (4) the FCC grain orientation (γ2). (**e**) Virtual dark-field images of $Fe_{1-x}O$ (left) and four differently oriented FCC Fe–Ni grains (γ1, γ2, γ3, and γ4), each with its corresponding SAED pattern. Insets include virtual apertures (red circles) for selected spots.

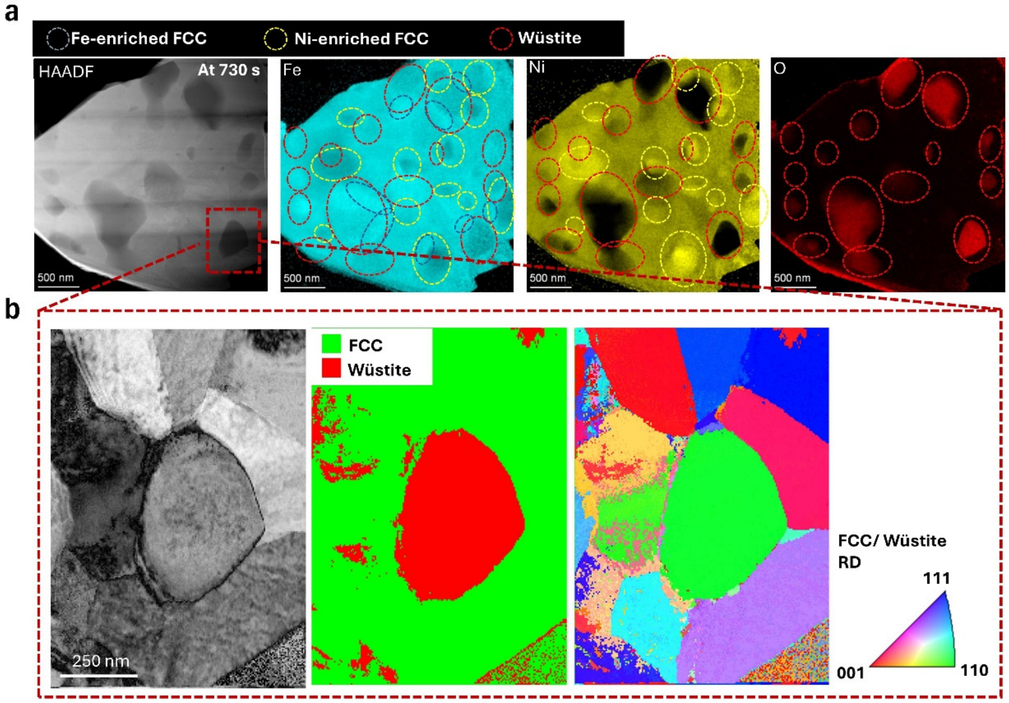

Fig. S4. (**a**) HAADF-STEM overview image examined after 730 s of hydrogen reduction of Fe_2O_3+ NiO (Fe–36Ni wt.%) at 700°C under a 0.6 L/h H_2 flow and the corresponding EDS maps of Fe (cyan), Ni (yellow), and O (red). Areas enriched in Fe-bearing FCC (blue outlines), Ni-bearing FCC (yellow outlines), and $Fe_{1-x}O$ (red outlines) are highlighted. (**b**) 4D-STEM results for the magnified view of the region marked in (a), showing a virtual bright-field TEM image (left), a phase map distinguishing FCC (green) from $Fe_{1-x}O$ (red) (middle), and an orientation map of FCC and $Fe_{1-x}O$ grains (right).

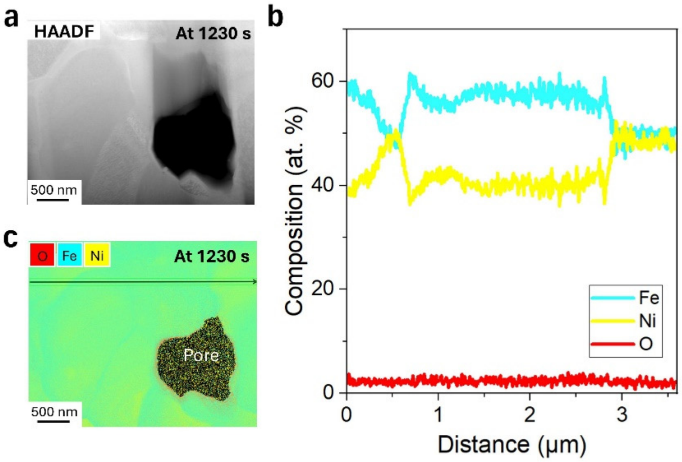

Fig. S5. (**a**) High-angle annular dark-field scanning transmission electron microscopy (HAADF-STEM) image at 1230 s of hydrogen reduction of Fe_2O_3+ NiO (Fe–36Ni wt.%) at 700°C under a 0.6 L/h H_2 flow showing the porous structure of the resulting alloy. (**b**) Corresponding energy-dispersive X-ray spectroscopy (EDS) elemental map confirming uniform Fe and Ni distribution within the porous region. (**c**) Line profile of elemental composition across the sample at 1230 s showing homogeneous Fe and Ni distribution, with a negligible oxygen content.

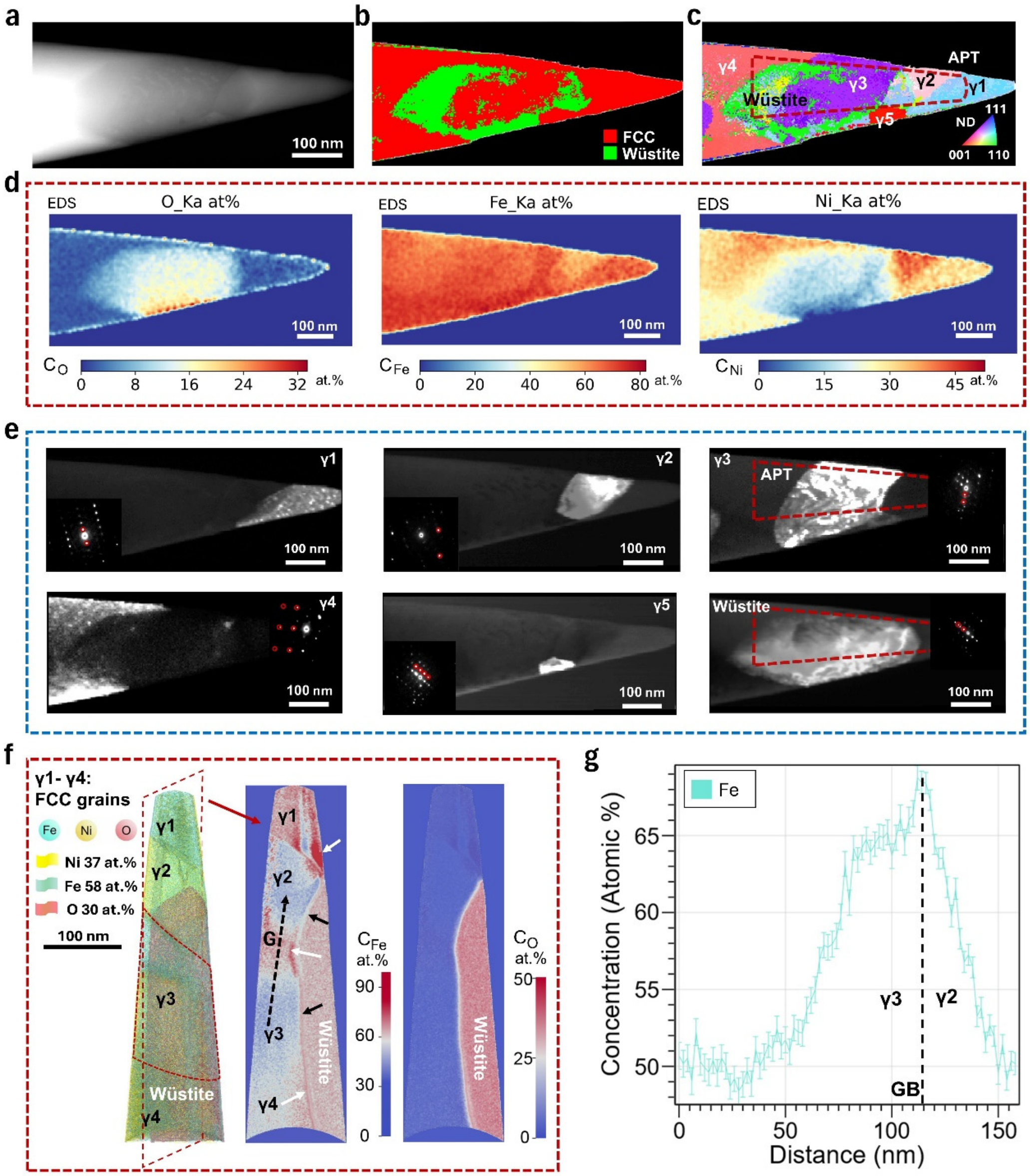

Fig. S6. (**a**) HAADF-STEM image of an APT needle acquired at 730 s of hydrogen reduction of Fe_2O_3+ NiO (Fe–36Ni wt.%) at 700°C under a 0.6 L/h H_2 flow, prepared to capture the $Fe_{1-x}O$–FCC interface. (**b**) Phase map of the same needle, showing $Fe_{1-x}O$ (green) embedded within the FCC Fe–Ni matrix (red). (**c**) Crystallographic orientation map (inverse pole figure) indicating multiple FCC grains (γ1–γ5) adjacent to the $Fe_{1-x}O$ region. (**d**) EDS elemental maps of the needle tip showing distributions of O (left), Fe (middle), and Ni (right). (**e**) Virtual dark-field STEM images of $Fe_{1-x}O$ and FCC grains (γ1–γ5), with selected area diffraction patterns (insets) confirming the phase identity. (**f**) 3D reconstruction of the APT dataset showing Ni (~37 at.%), Fe (~58 at.%), and residual O (~30 at.%) concentrations. The left panel identifies FCC grains γ1–γ4 adjacent to $Fe_{1-x}O$. Middle and right panels show elemental distributions of Fe and O of the slice (the red dashed box in the left panel). The white arrows show the enrichment of Fe. (**g**) One-dimensional Fe concentration profile across the γ3–γ2 interface, taken along the dashed arrow in (f), showing compositional variation across the grain boundary.

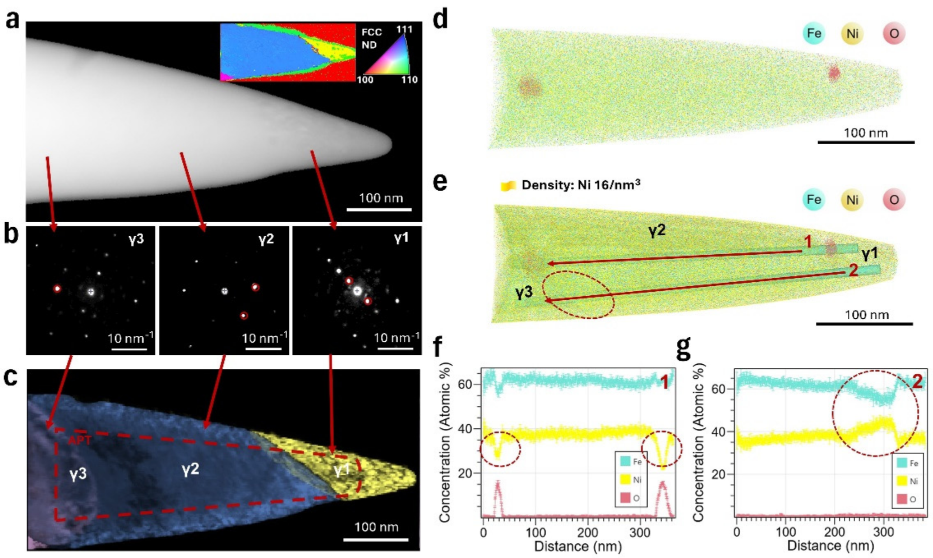

Fig. S7. (**a**) HAADF-STEM image of the APT tip from a region where oxides were nearly fully reduced at 730 s of hydrogen reduction of Fe_2O_3+ NiO (Fe–36Ni wt.%) at 700°C under a 0.6 L/h H_2 flow. The inset shows an inverse pole figure map (color-coded by crystal direction) overlaid on the tip apex, obtained by indexing the 4D-STEM dataset, confirming that the tip contains multiple FCC grains (γ1, γ2, and γ3). (**b**) Corresponding 4D-STEM electron diffraction patterns from the three γ grains, with key reflections circled to produce virtual dark-field images. (**c**) Overlay of these virtual dark-field images for each FCC grain and orientation, highlighting the spatial arrangement of γ1 (yellow), γ2 (blue), and γ3 (purple). The dashed red box outlines the region subsequently analyzed by APT. (**d**) Reconstructed APT point cloud, showing the distributions of Fe (cyan), Ni (yellow), and O (pink). Two oxide-rich zones (red) are evident within the matrix. (**e**) The same dataset, now with a semitransparent Ni isodensity surface (16 nm^{-3}), to reveal potential grain boundaries. Labels "1" and "2" mark the paths along which 1D composition profiles were extracted. (**f**, **g**) Composition profiles taken along paths 1 and 2, respectively, in (e). Path 1 shows Ni-depleted zones (circled in red) near oxide pockets; the O concentration rises as Ni decreases, indicating residual oxide locations. Path 2 reveals the remaining precursor high-Ni region (circled in red). APT results (fig. S7) reveal the presence of fine residual $Fe_{1-x}O$ at the γ1/γ2 and γ2/γ3 grain boundaries, as highlighted by the Ni density isosurface in fig. S7e, which illustrates the growth of FCC (Fe, Ni) grains through the consumption of $Fe_{1-x}O$. In fig. S7f, a thin Fe-enriched layer near the oxide interface indicates an ongoing reaction. In the closed area, these oxide remnants are expected to undergo further reduction in later rate-limiting stages through diffusion of O. The reduction of residual oxides proceeds slowly—leading to additional hydrogen consumption and higher energy requirements to sustain reaction temperatures. A comparison of figs. S7e and S7g shows that, even within the same γ_2 grain, a region near the γ2/γ3/ $Fe_{1-x}O$ triple junction exhibits elevated Ni levels, implying that Fe diffusion toward the γ_2 precursor portion is slower than direct Fe precipitation and alloying in other parts of the γ2 grain.